Arch. Metall. Mater. **67** (2022), 4, 1491-1495

DOI: https://doi.org/10.24425/amm.2022.141080

SANG-GYU KIM[1], YOUNG-CHUL YOON[1], SEOK-WOO KO[1], BYOUNGCHUL HWANG[1*]

EFFECT OF PRE-STRAIN ON HYDROGEN EMBRITTLEMENT IN INTERCRITICALLY ANNEALED Fe-6.5Mn-0.08C MEDIUM-MN STEELS

The present research deals with the effect of pre-strain on the hydrogen embrittlement behavior of intercritically annealed medium-Mn steels. A slow strain-rate tensile test was conducted after hydrogen charging by an electrochemical permeation method. Based on EBSD and XRD analysis results, the microstructure was composed of martensite and retained austenite of which fraction increased with an increase in the intercritical annealing temperature. The tensile test results showed that the steel with a higher fraction of retained austenite had relatively high hydrogen embrittlement resistance because the retained austenite acts as an irreversible hydrogen trap site. As the amount of pre-strain was increased, the hydrogen embrittlement resistance decreased notably due to an increase in the dislocation density and strain-induced martensite transformation.

Keywords: Medium-manganese steel; Hydrogen embrittlement; Electrochemical charging; Pre-strain; Slow strain-rate tensile (SSRT) test

1. Introduction

In order to reduce carbon emissions and improve collision safety in the automobile industry, the third-generation advanced high-strength steels have been developed [1-6]. Among them, medium-Mn steel containing normally 4 to 10 wt.% Mn is regarded as one of the most promising candidate owing to its good combination of high strength and ductility [7-10]. For hot-rolled medium-Mn steel sheets, intercritical annealing in the two-phase ($\alpha + \gamma$) region has generally been adopted as a heat treatment practice to obtain an attractive duplex microstructure of ultra-fine grained ferrite and retained austenite [9]. The excellent mechanical properties of medium-Mn steels originate from the transformation-induced plasticity effect during deformation, which depends mainly on the fraction and stability of retained austenite [11]. However, most advanced high-strength steels, including medium-Mn steel, are vulnerable to hydrogen embrittlement [12-16]. Thus, it is important to evaluate the susceptibility to hydrogen embrittlement of these steels for predicting potential hydrogen damage. It has been found that almost all types of defects in steels can act as hydrogen trap sites, which can be generally classified into reversible and irreversible trap sites according to their trap activation energy [17].

On the other hand, it is also important to investigate the effects of pre-strain on hydrogen embrittlement behavior in medium-Mn steels because automotive steels such as medium-Mn steels are commonly subjected to a forming process accompanied by plastic deformation. Wang et al. [18] found that the reversible hydrogen content of cold-rolled Al-containing medium-Mn steel increases remarkably with an increase in the amount of pre-strain. All of these factors can lead not only to high residual stress but also to the transformation of retained austenite to martensite depending on its stability. Therefore, in this study, the effects of pre-strain on the hydrogen embrittlement behavior of the medium-Mn steels with different amounts of retained austenite are investigated in terms of austenite stability and hydrogen trapping.

2. Experimental

The chemical composition of the medium-Mn steel used in this study is Fe-0.08C-6.5Mn-0.1Si-0.3Al (wt.%). After an ingot was melted in a vacuum-induction furnace and homogenized at above 1,200°C, it was hot-rolled at 900°C to a thickness of 12 mm. The steel was then austenitized at 900°C for 60 min,

[1] SEOUL NATIONAL UNIVERSITY OF SCIENCE AND TECHNOLOGY, DEPARTMENT OF MATERIALS SCIENCE AND ENGINEERING, SEOUL, 01811, REPUBLIC OF KOREA

* Corresponding author: bhwang@seoultech.ac.kr

followed by water quenching. After austenitization, the steel was intercritically annealed at 500°C and 600°C for 60 min, respectively. The intercritical annealing temperatures were determined as a temperature between equilibrium eutectoid (A_{e1}) and ferrite start (A_{e3}) temperatures, which were calculated using Thermo-Calc software with TCFE7 database. For convenience, the steels are referred to as the 'IA500' and 'IA600' steels according to the difference in the intercritical annealing temperature.

The microstructures of both the IA500 and IA600 steels were examined using an electron backscattered diffractometer (EBSD, model: TSL Hikari XP, AMETEK, USA) equipped with a field-emission scanning electron microscope (FE-SEM, model: JSM-7100F, JEOL, Japan). Specimens for the EBSD observation were polished using a suspension of 0.04 μm colloidal silica particles and were electro-polished in a mixed solution of 90% glacial acetic acid (CH_3COOH) and perchloric acid ($HClO_4$) to remove a mechanically damaged layer. The volume fraction of the retained austenite in the intercritically annealed steels was determined using X-ray diffractometer (XRD, model: Bruker DE/D8 Advance, Bruker, Germany) with a CuKα target (λ = 1.5405Å). The scanning range, rate and step size were 40°~100°, 2° min^{-1} and 0.02°, respectively.

Sub-sized plate-type tensile specimens (ASTM E8 standard) were processed perpendicular to the rolling direction. The thickness, width and length of the gauge part were 2.0 mm, 6.3 mm and 25.0 mm, respectively. The tensile test was conducted with a slow strain-rate of 5×10^{-5} s^{-1} at room-temperature using a universal testing machine with a capacity of ten tons (model: UT-100E, MTDI, Korea). Some of the tensile specimens were electrochemically hydrogen charged in an aqueous solution of 3 wt.% NaCl and 0.3 wt.% NH_4SCN with a current density of 50 Am^{-2} for 24 hr using a Pt wire as a counter electrode. After the tensile test, fractured tensile specimens were observed using a stereo microscope (model: SMZ745T, Nikon, Japan) and SEM (model: EVO10, Carl Zeiss, Germany).

3. Results and discussion

Fig. 1 presents the EBSD inverse pole figure (IPF), image quality (IQ), phase maps and XRD analysis results of the IA500 and IA600 steels. Both steels exhibited a lath-type complex microstructure with ferrite, martensite and austenite (Fig. 1(a)). The retained austenite formed at the boundaries of martensite blocks occurred prior to the recrystallization of the martensite matrix [9]. To measure the volume fraction of retained austenite after intercritical annealing, XRD analysis was conducted using electro-polished specimens (Fig. 1(b)). In the results of a Rietveld refinement analysis, the IA500 and IA600 steels showed retained austenite of 0.5 vol.% and 9.8 vol.%, respectively. The IA600 steel had a relatively large amount of retained austenite at the prior austenite grain boundary and martensite lath boundary due to the relatively high intercritical annealing temperature [19,20].

Engineering stress-strain curves of the *H*-charged and non-charged specimens are shown in Fig. 2. As the amount of

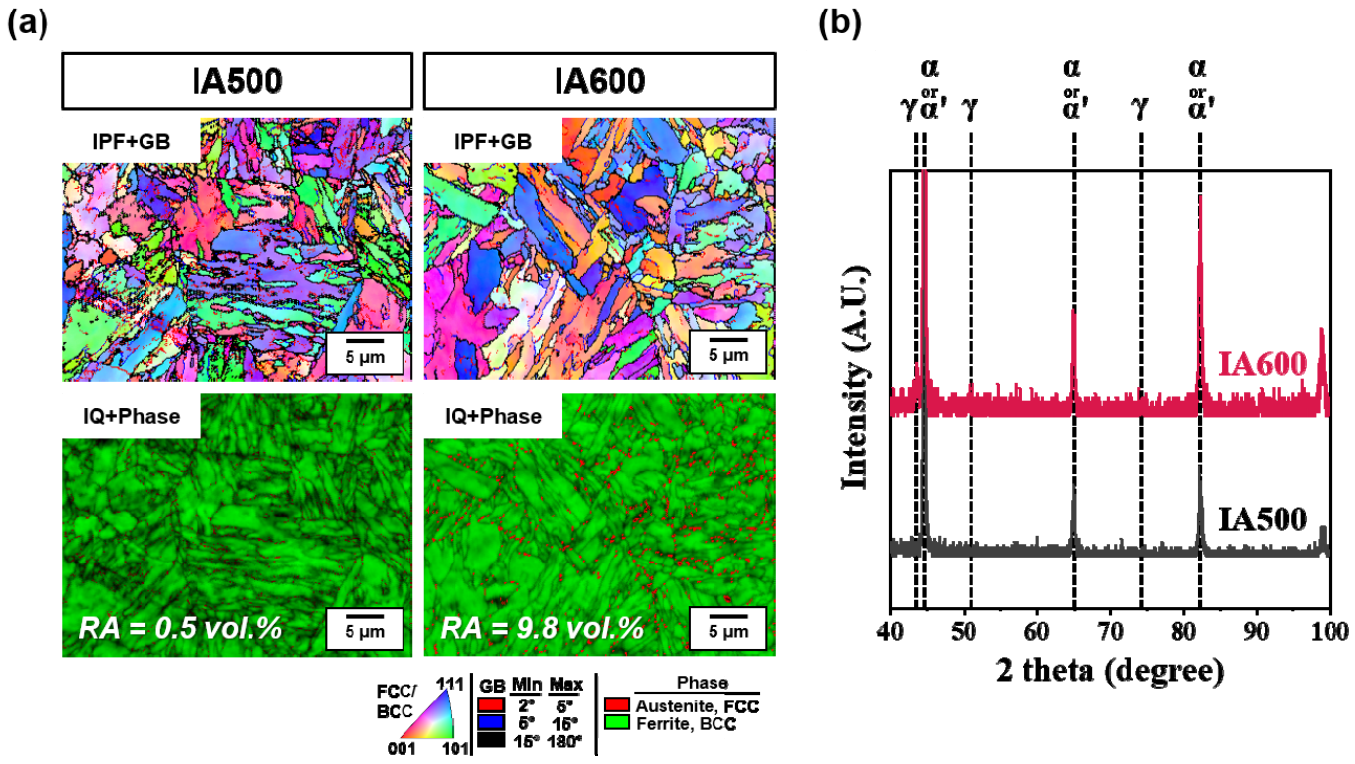

Fig. 1. Electron backscatter diffraction (EBSD) analysis of the IA500 and IA600 steels intercritically annealed at 500°C and 600°C, respectively. (a) inverse pole figure (IPF) maps indicated different color codes according to Miller indexes and phase maps colored in green and red corresponding to the ferrite or martensite (α or α') and retained austenite (RA), respectively. (b) X-ray diffraction (XRD) patterns of the IA500 and IA600 steels. The dashed lines represent ferrite (α) and austenite (γ) peaks according to the diffraction planes

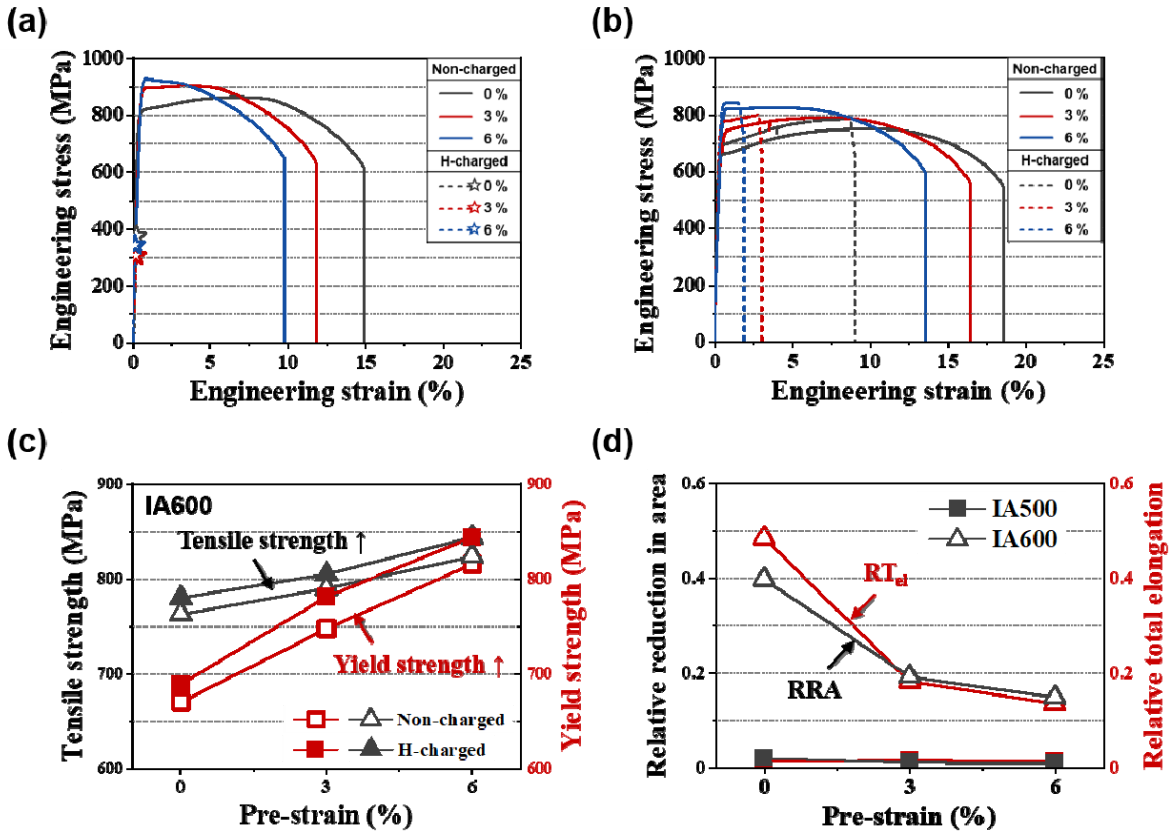

Fig. 2. Slow strain-rate tensile (SSRT) test results of the IA500 and IA600 steels intercritically annealed at 500°C and 600°C, respectively. Engineering stress-strain curves according to hydrogen charging and pre-strain conditions of the (a) IA500 steel and (b) IA600 steel; (c) changes in yield and tensile strength of IA600 steel and (d) relative reduction of area (RRA) and relative total elongation (RT_{el}) values of both steels

pre-strain was increased, yield and tensile strength increased and total elongation decreased due to the work hardening effect [21]. In particular, the *H*-charged IA500 steel specimens revealed a premature fracture in the elastic region before necking occurred regardless of the amount of pre-strain (Fig. 2(a)). However, the *H*-charged IA600 steel specimens showed higher hydrogen embrittlement resistance than the IA500 steel (Fig. 2(b)). For a comparative evaluation of hydrogen embrittlement resistance, relative total elongation (RT_{el}) and relative reduction of area (RRA) were calculated by the following equations:

$$\text{Relative total elongation}\left(RT_{el}\right) = \\ = \frac{\text{Total elongation}_{H-\text{charged}}}{\text{Total elongatoin}_{Non-\text{charged}}} \quad (1)$$

$$\text{Relative reduction of area}\left(\text{RRA}\right) = \\ = \frac{\text{Redution of area}_{H-\text{charged}}}{\text{Redution of area}_{Non-\text{charged}}} \quad (2)$$

The IA500 steel showed very low RT_{el} and RRA values of nearly zero under all pre-strain conditions, whereas the RT_{el} and RRA values for the IA600 steel tended to decrease gradually as the amount of pre-strain was increased (Fig. 2(d)). The retained austenite formed by intercritical annealing acts as an irreversible hydrogen trap site to immobilize diffusible hydrogen, thereby increasing the hydrogen embrittlement resistance [22]. In addition, the RT_{el} and RRA values gradually decreased with an increase in the amount of pre-strain, which can be considered as an effect of the increase in the dislocation density and strain-induced martensite formation [18]. Meanwhile, the IA600 steel presented an improvement in yield and tensile strength after hydrogen charging, resulting from the effect of solid solution strengthening by hydrogen atoms (Fig. 2(c)) [23,24].

Fig. 3 presents the tensile fractured surfaces of IA500 and IA600 steels using a stereo microscope. The *H*-charged IA500 steel specimens had a brittle fracture region of almost 100% regardless of the pre-strain condition. On the other hand, it can be seen that the brittle fracture region of *H*-charged IA600 steel specimens gradually increased as the amount of pre-strain was increased.

To clarify the cause of premature fracture of the IA500 and IA600 steels, the tensile fractured surfaces were observed using SEM (Fig. 4). Whereas the non-charged specimens revealed ductile fracture behavior including dimples, the *H*-charged specimens exhibited brittle fracture behavior and cracks propagating along the prior austenite grain boundary and martensite lath boundary. In the *H*-charged IA500 steel specimens, cracks propagated rapidly along the prior austenite grain boundary and martensite lath boundary, indicating flat intergranular fracture surfaces. Diffusive hydrogen trapped in the prior austenite grain boundary and martensite lath boundary weakens the lattice

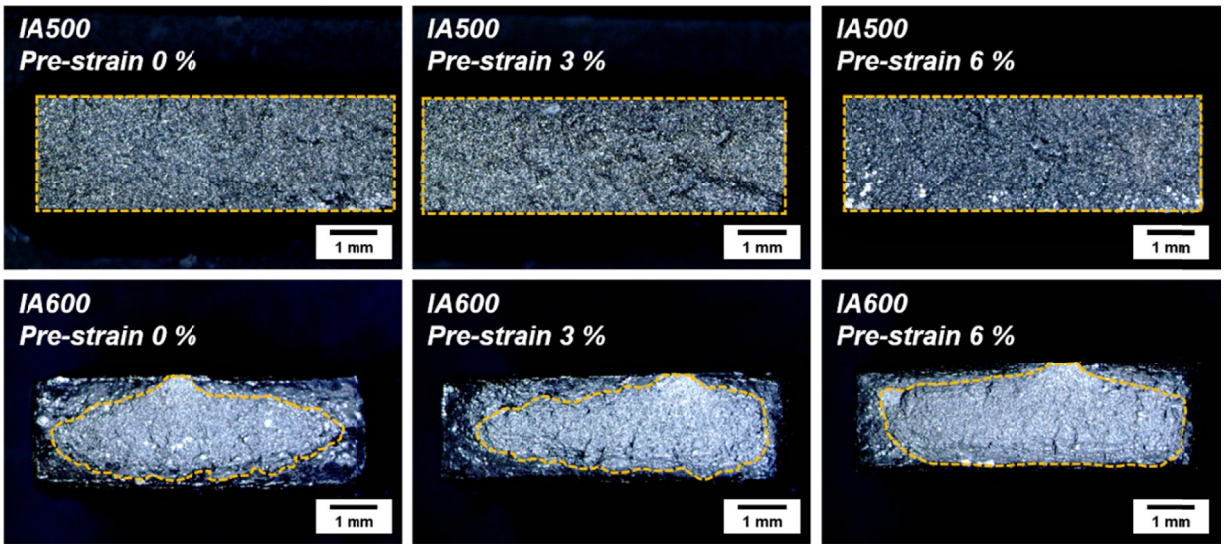

Fig. 3. Stereo microscope fractographs of the tensile fractured surfaces of the hydrogen charged IA500 and IA600 steels intercritically annealed at 500°C and 600°C, respectively. The yellow dashed boxes indicate brittle fractured regions

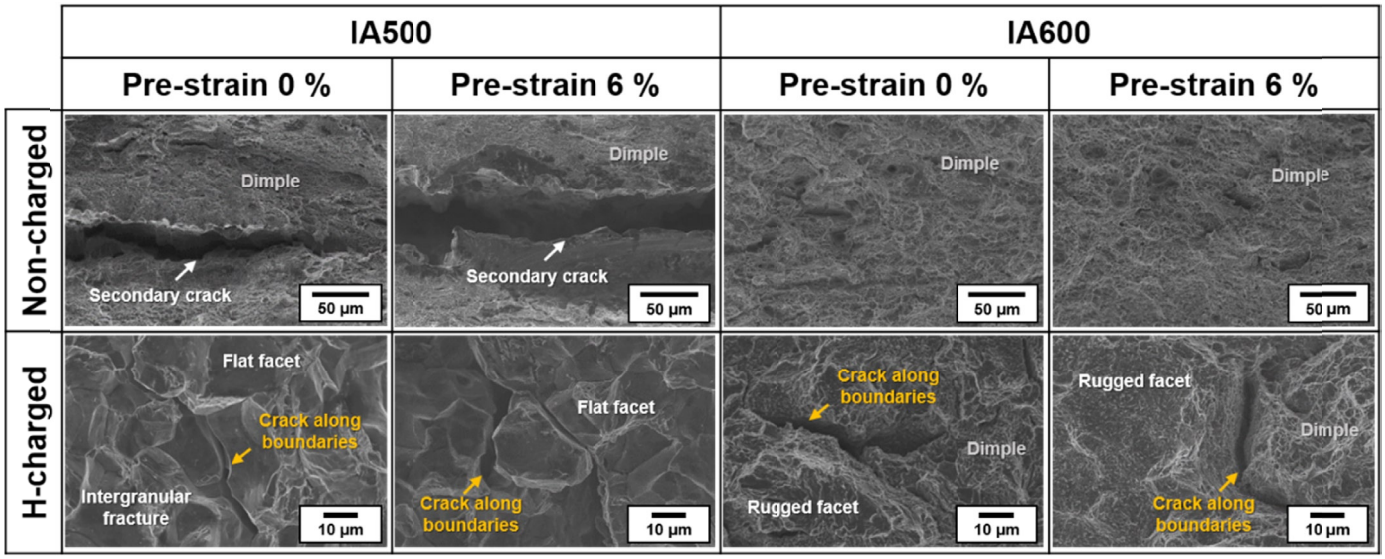

Fig. 4. Scanning electron microscope (SEM) fractographs of the tensile fractured surfaces of the IA500 and IA600 steels intercritically annealed at 500°C and 600°C, respectively

bonding force [22,25]. The *H*-charged IA600 steel specimens also showed crack propagation along the prior austenite grain boundary and martensite lath boundary, though some ductile fracture behavior with dimples was also observed. Since the retained austenite acted as an irreversible hydrogen trap site, the fracture surface had a rugged surface.

From these results, it can be understood that retained austenite in medium-Mn steels is able to act as a beneficial hydrogen trap site to immobilize the diffusible hydrogen and thus to improve the hydrogen embrittlement resistance. This is because the α/γ interface serves as a strong trap and due to the lower hydrogen diffusivity and high solubility of hydrogen in austenite. On the other hand, the decreased hydrogen embrittlement resistance stemmed from an increase in the dislocation density and strain-induced martensite formation in accordance with an increase in the amount of pre-strain.

4. Conclusions

Based on the present investigation of the effect of pre-strain on the hydrogen embrittlement of two intercritically annealed Fe-0.08C-6.5Mn-0.1Si-0.3Al medium-Mn steels with different fractions of retained austenite, the following conclusions can be drawn.

1. The microstructure of intercritically annealed medium-Mn steels exhibited a lath-type complex microstructure with ferrite, martensite and retained austenite. The steel with a higher intercritical annealing temperature had a relatively large amount of retained austenite due to its high austenite stability.
2. The medium-Mn steel with a higher fraction of retained austenite showed a better hydrogen embrittlement resistance than that with a lower fraction of retained austenite

because the retained austenite formed during intercritical annealing acts as an irreversible trap site for hydrogen.

3. With an increase in the amount of pre-strain, the hydrogen embrittlement resistance of intercritically annealed medium-Mn steels decreased due to an increase in the dislocation density and strain-induced martensite transformation, acting as a reversible trap sites vulnerable to hydrogen embrittlement.

Acknowledgments

The present study was supported by the Basic Science Research Program through the National Research Foundation of Korea, South Korea (NRF-2022R1A2C2004834) and by the Technology Innovation Program through the Ministry of Trade, Industry and Energy (MOTIE), South Korea (Grant No. 20015945).

REFERENCES

[1] M. Takahashi, ISIJ Int. **55**, 79-88 (2015).
[2] S.I. Lee, J. Lee, B. Hwang, Mater. Sci. Eng. A **758**, 56-59 (2019).
[3] S.I. Lee, S.Y. Lee, J. Han, B. Hwang, Mater. Sci. Eng. A **742**, 334-343 (2019).
[4] S.I. Lee, S.Y. Lee, S.G. Lee, H.G. Jung, B. Hwang, Met. Mater. Int **24**, 1221-1231 (2018).
[5] S.Y. Lee, S.I. Lee, B. Hwang, Mater. Sci. Eng. A **711**, 22-28 (2018).
[6] J. Tian, G. Xu, Z. Jiang, H. Hu, Q. Yuan, X. Wan, Met. Mater. Int **26**, 961-972 (2020).
[7] Y.K. Lee, J. Han, Mater. Sct. Technol. **31**, 843-856 (2015).
[8] D.W. Suh, S.J. Kim, Scripta Mater. **126**, 63-67 (2017).
[9] J. Han, S.J. Lee, J.G. Jung, Y.K. Lee, Acta Mater. **78**, 369-377 (2014).
[10] D.W. Suh, J.H. Ryu, M.S. Joo, H.S Yang, K. Lee, H.K.D.H. Bhadeshia, Metall. Mater. Trans. A **33**, 286-293 (2013).
[11] H.S. Wang, G. Yuan, M.F. Lan, J. Kang, Y.X. Zhang, G.M. Cao, R.D.K. Misra, G.D. Wang, J. Mater. Sci. **53**, 12570-12582 (2018).
[12] S.K. Dwivedi, M. Vishwakarma, Int. J. Hydrog. **43**, 21603-21616 (2018).
[13] J.H. Ryu, Y.S. Chun, C.S. Lee, H.K.D.H. Bhadeshia, D.W. Suh, Acta Mater. **60**, 4085-4092 (2012).
[14] M. Wang, C.C. Tasan, M. Koyama, D. Ponge, D. Raabe, Metall. Mater. Trans. A **46**, 3797-3802 (2015).
[15] M. Asadipoor, J. Kadkhodapour, A.P. Anaraki, S.M.H. Sharifi, A.Ch. Darabi, A. Barnoush, Met. Mater. Int. **27**, 2276-2291 (2021).
[16] A.I. Hwang, D.G. Lee, Y. Jung, J.M. Koo, J.D. Cho, J.S. Lee, D.W. Suh, Met. Mater. Int. **27**, 3959-3967 (2021).
[17] Q. Liu, Q. Zhou, J. Venezuela, M. Zhang, J. Wang, A. Atrens, Corros. Rev. **34**, 127-152 (2016).
[18] J.J. Wang, W. Hui, Z. Xie, Z. Wang, Y. Zhang, X. Zhao, Int. J. Hydrog. **45**, 22080-22093 (2020).
[19] Y.G. Yang, Z.L. Mi, M. Xu, Q. Xiu, J. Li, H.T. Jiang, Mater. Sci. Eng. A **725**, 389-397 (2018).
[20] C.W. Shao, W.J. Hui, Y.J. Zhang, X.L. Zhao, Y.Q. Weng, Mater. Sci. Eng. A **682**, 45-53 (2017).
[21] G.E. Dieter, McGraw-Hill, Mechanical Metallurgy, London 1988.
[22] J. Han, J.H. Nam, Y.K. Lee, Acta Mater. **113**, 1-10 (2016).
[23] A.J. West, M.R. Louthan, Mater. Trans. A **13**, 2049-2058 (1982).
[24] T. Zakroczymski, A. Glowacka, W. Swiatnicki, Corros. Sci. **47**, 1403-1414 (2005).
[25] G.P. Tiwari, A. Bose, J.K. Chakravartty, S.L. Wadekar, M.K. Totlani, R.N. Arya, R.K. Fotedar, Mater. Sci. Eng. A **286**, 269-281 (2000).